Journal of
*Marine Science and Engineering*

*Article*

# A New Multi-Mechanism Synergistic Acoustic Structure for Underwater Low-Frequency and Broadband Sound Absorption

**Kangkang Shi [1,2], Dongsheng Li [1,2], Dongsen Hu [1,2], Qi Shen [1,2] and Guoyong Jin [3,*]**

1 National Key Laboratory of Ship Vibration and Noise, China Ship Scientific Research Center, Wuxi 214082, China; shikk@cssrc.com.cn
2 Taihu Laboratory of Deepsea Technological Science, Wuxi 214082, China
3 College of Power and Energy Engineering, Harbin Engineering University, Harbin 150001, China
* Correspondence: guoyongjin@hrbeu.edu.cn

**Abstract:** The acoustic absorption characteristics of anechoic coatings attached to the surface of underwater vehicles are closely related to their acoustic stealth. Owing to the essential property of local resonance, the narrow sound-absorption band cannot meet the underwater broadband sound absorption requirements. To this end, a multi-mechanism synergistic composite acoustic structure (MMSC−AS) was designed according to the integration of multiple acoustic dissipation mechanisms in this paper. Then, the acoustical calculation model for MMSC−AS was developed by using the graded finite element method (G-FEM), and the feasibility and the correctness of the established acoustical calculation model were verified. The underwater sound absorption behaviors of MMSC−AS were studied, and the optimization of the sound absorption characteristics of the MMSC−AS was also carried out. The results indicated that the calculation accuracy of the G-FEM was better than that of the FEM under the condition of the same mesh elements. Moreover, there were many sound wave regulation mechanisms in the MMSC−AS, and the synergy between the mechanisms enriched the mode of sound acoustic energy dissipation, which could widen the absorption band with effect. This study provides theoretical and technical basis for breaking through the challenge of low-frequency and broadband acoustic structure design of underwater vehicles.

**Keywords:** underwater sound absorption; multi-mechanism synergistic; low-frequency broadband; graded finite element method



**Citation:** Shi, K.; Li, D.; Hu, D.; Shen, Q.; Jin, G. A New Multi-Mechanism Synergistic Acoustic Structure for Underwater Low-Frequency and Broadband Sound Absorption. *J. Mar. Sci. Eng.* **2023**, *11*, 2373. https://doi.org/10.3390/jmse11122373

Academic Editor: Erkan Oterkus

Received: 27 October 2023
Revised: 8 December 2023
Accepted: 13 December 2023
Published: 15 December 2023



## 1. Introduction

The anechoic coating is a key technology that can simultaneously suppress the structural echo and vibro-acoustic response, and it is widely used in acoustic stealth technology for underwater vehicles. With the advancement of active sonar detection [1,2], the detection level of active sonar is constantly improving, and the detection frequency band is gradually expanding to a low frequency. Nevertheless, for the conventional acoustical structure, it is difficult to meet the requirements of acoustic stealth for underwater vehicles, so the acoustic structure with perfect low-frequency and broadband sound absorption is the key to improving and optimizing the acoustic target intensity of underwater vehicles.

Rubber, polyurethane, and other polymer materials are widely used in traditional anechoic coating, and sound waves can be absorbed by the friction of molecular segments inside the viscoelastic material that dissipates the energy of sound waves. According to different acoustic structures and acoustic absorption mechanisms, underwater acoustic structures can be classified as homogeneous polymer acoustic materials [3–5], particle-filled acoustic structures [6–8], cavity resonance acoustic structures [9–11], and gradient acoustic structures [12–14].

The proposal of phononic crystals (PCs) has provided novel research means for the control of low-frequency acoustic waves in recent years [15,16]. Afterward, Li et al. [17]

designed a new type of acoustic structure composed of soft rubber localized vibrators distributed in the water matrix, and the concept of acoustical metamaterials was explicitly proposed. Acoustic metamaterials (AMs) are artificial materials with extraordinary acoustic properties possessed by natural materials, such as the negative equivalent mass density [18,19]. AMs exhibit new physical effects, which can be used to regulate the refraction, scattering, and absorption of sound waves, thereby achieving different acoustic functions, and have good application prospects [20–26]. Veselago et al. [27–29] studied the wave propagation properties of waves in metamaterials and materials with a negative index of refraction, also called left-handed or metamaterials, and the extraordinary physical properties of metamaterials were further explained.

The application of AMs also is extended to the study of underwater acoustic properties due to the favorable acoustic properties of AMs in air. Based on the extraordinary physical properties of AMs, many studies on the acoustic properties of AMs have been carried out. Zhao et al. [30–35] revealed the sound-absorption mechanism of PCs and systematically studied the regulation of the sound absorption performance of local resonance PCs. Zhang et al. [36–38] embedded a periodic thin-plate into two layers of rubber, which significantly broadened the sound absorption band. Jiang and Chen [39–42] designed a locally resonant phononic woodpile and studied the bandgap and acoustic characteristics of the phononic woodpile structure. Gao et al. [43–45] designed many types of AMs and achieved excellent underwater acoustic characteristics. In addition, many experimental studies on the underwater acoustic absorption performance of acoustic metamaterials have been conducted [46–48], and it was further demonstrated that acoustic metamaterials had excellent underwater sound absorption performance.

Low-frequency sound waves can be controlled by the physical characteristics of AMs, which provides a novel technical direction for the design of new small-scale anechoic coatings. However, the narrow absorption band restricts its underwater acoustic absorption application for its intrinsic physical properties inside AMs. From the perspective of the sound absorption mechanism, how to broaden the absorption band of AMs and achieve strong sound absorption simultaneously is the key to achieving underwater low-frequency and broadband sound absorption. Generally, the means to widen the absorption band of AMs are limited at present, so it is necessary to conduct further investigation on the acoustic mechanism of broadband sound absorption. In this paper, a new type of MMSC−AS is designed considering the multi-mechanism synergistic effect in an effort to improve narrowband sound absorption, such as local resonance, multi-resonator coupling resonance, cavity resonance, and functionally graded materials (FGMs). The G-FEM is employed to develop the acoustic model of the MMSC−AS, and the feasibility of establishing acoustic models by the G-FEM is verified. On this basis, the underwater sound absorption behaviors and mechanism of MMSC−AS are studied, and the regulation law of the MMSC−AS is explored. Finally, the sound absorption characteristics of the MMSC−AS are optimized in terms of material and geometric parameters.

## 2. Acoustic Model and Calculation Method

### 2.1. Model of MMSC−AS

Considering the cavity resonance acoustic structure (CRAS), multi-resonator coupling resonance acoustic structure (MCRAS), and FGMs, the MMSC−AS was devised by combining with the sound characteristics of the three acoustic structures. A diagram of the underwater sound-absorption physical model of the MMSC−AS is shown in Figure 1. It can be observed that the matrix was composed of gradient layers 1 and 2, wherein gradient layer 1 contained multi-layered spherical resonators and cylindrical cavities and gradient layer 2 contained the single spherical resonators and cylindrical cavities. In addition, the multi-layered resonators were connected with each other through the coating layers, and the resonators and cavities were alternately and periodically arranged along the $x$ direction, and the resonators (or cavities) arranged periodically along the $y$ direction. The MMSC−AS was applied on the surface of the steel plate, and the other side of the steel plate, there was a semi-infinite water domain. The sound wave incidents were vertically along the thickness of the MMSC−AS.

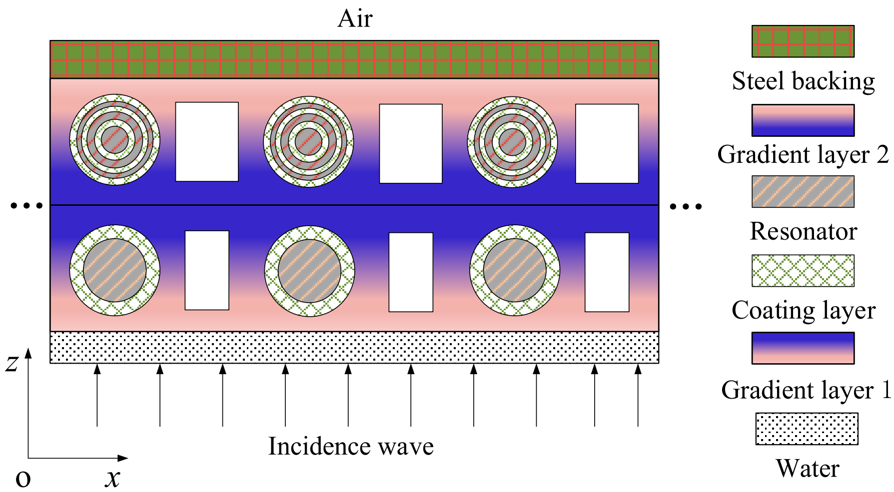


**Figure 1.** Underwater physical model of the MMSC−AS.

A diagram of a unit cell of the MMSC−AS on the *xoz* plane is shown in Figure 2. The thickness of gradient layer 1 is $h_1$, and the radii of the multi-layered coating layers and spherical resonators are $r_i$ ($i$ = 1–6). The height and radius of the cylindrical cavity are $h_{c1}$ and $r_{c1}$, respectively. The thickness of gradient layer 2 is $h_2$, and the radii of the single spherical resonator and coating layer are $r_7$ and $r_8$, respectively. The height and radius of the cylindrical cavity are $r_{c2}$ and $h_{c2}$, respectively. Additionally, the thickness of the steel plate is $h_s$, and the distance between adjacent cavities in each layer is $a_1 + a_2$. The FGMs proposed in this paper were synthesized from epoxy and inorganic fillers. The gradient indices of gradient layers 1 and 2 are $P_1$ and $P_2$, respectively. The materials of the coating layer and resonators are soft rubber and steel, respectively.

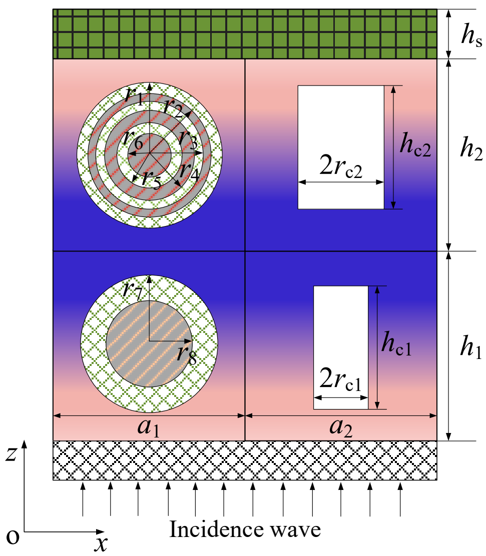


**Figure 2.** Cross-sectional view of a unit cell of the MMSC−AS on the *xoz* plane.

### 2.2. Acoustic Calculation Model for MMSC−AS

Assuming that the fluid satisfies incompressibility and uniformity, the wave equation is:

$$\frac{1}{c^2}\frac{\partial^2 p}{\partial t^2} - \nabla^2 p = 0 \quad (1)$$

where $c$ donates sound speed, $p$ is sound pressure, and $t$ is time.

The equation can be expressed by finite element discretization for the fluid domain [43]:

$$\mathbf{M}_f\ddot{\mathbf{p}} + \mathbf{K}_f\mathbf{p} + \rho_0\mathbf{R}\ddot{\mathbf{u}} = \mathbf{f} \tag{2}$$

where $\mathbf{K}_f$ and $\mathbf{M}_f$ are the stiffness matrix and mass matrix, $\mathbf{p}$ is the sound pressure vector, R describes the fluid–structure coupling, $\mathbf{u}$ is the node displacement of the structure at the fluid–structure coupling surface, $\mathbf{f}$ is the fluid load vector, and $\rho_0$ is the density of water.

The relationship between the stress $\sigma$ and strain $\varepsilon$ can be written as [49]:

$$\begin{bmatrix} \sigma_x \\ \sigma_y \\ \sigma_z \\ \sigma_{yz} \\ \sigma_{xz} \\ \sigma_{xy} \end{bmatrix} = \begin{bmatrix} C_{11} & C_{12} & C_{13} & 0 & 0 & 0 \\ C_{12} & C_{22} & C_{23} & 0 & 0 & 0 \\ C_{13} & C_{23} & C_{33} & 0 & 0 & 0 \\ 0 & 0 & 0 & C_{44} & 0 & 0 \\ 0 & 0 & 0 & 0 & C_{55} & 0 \\ 0 & 0 & 0 & 0 & 0 & C_{66} \end{bmatrix} \begin{bmatrix} \varepsilon_x \\ \varepsilon_y \\ \varepsilon_z \\ \varepsilon_{yz} \\ \varepsilon_{xz} \\ \varepsilon_{xy} \end{bmatrix} \tag{3}$$

where $C_{ij}$ are stiffness factors related to coordinates, which can be written as:

$$C_{11} = C_{22} = C_{33} = \lambda(x,y,z) + 2\mu(x,y,z) \tag{4}$$

$$C_{12} = C_{13} = C_{23} = \lambda(x,y,z) \tag{5}$$

$$C_{44} = C_{55} = C_{66} = \mu(x,y,z) \tag{6}$$

where $\lambda$ and $\mu$ are Lame constants.

The Lagrange functional of FGAS can be determined based on kinetic energy $T$ and $U$:

$$L = T - U + W + W_f \tag{7}$$

where $W_f$ is the work performed by the fluid load and $W$ is the work performed by mechanical loads.

Equation (7) can be expressed as follows according to Hamilton's principle:

$$\delta\int_{t_0}^{t_1}\left(T - U + W + W_f\right)dt = 0 \tag{8}$$

By variating Equation (8), we can obtain:

$$\mathbf{M}_s\ddot{\mathbf{u}} + \mathbf{K}_s\mathbf{u} - \mathbf{R}^{\mathrm{T}}\mathbf{p} = \mathbf{F}_m \tag{9}$$

where $\mathbf{K}_s$ and $\mathbf{M}_s$ are the stiffness matrix and mass matrix of the structure and $\mathbf{F}_m$ is the mechanical load vector.

The mass matrix and the stiffness matrix are derived as:

$$\mathbf{M}_s = \sum_1^e \mathbf{M}_s^e = \sum_1^e \iiint\limits_{V_e} \mathbf{S}^T\rho(x,y,z)\mathbf{S}dV_e \tag{10}$$

$$\mathbf{K}_s = \sum_1^e \mathbf{K}_s^e = \sum_1^e \iiint\limits_{V_e} \mathbf{B}_\delta^{\mathrm{T}}\mathbf{C}(x,y,z)\mathbf{B}_\delta dV_e \tag{11}$$

where $\mathbf{S}$ is the shape function vector of structural elements and $\mathbf{B}_\delta$ represents the first-order partial derivative vector of the shape function.

The acoustic–solid coupling equation of the FGAS can be given by:

$$\begin{bmatrix} \mathbf{K}_s - \omega^2\mathbf{M}_s & -\mathbf{R}^T \\ -\rho_0\omega^2\mathbf{R} & \mathbf{K}_f - \mathbf{C}_\phi - \omega^2\mathbf{M}_f \end{bmatrix} \begin{Bmatrix} \mathbf{u} \\ \mathbf{p} \end{Bmatrix} = \begin{Bmatrix} \mathbf{F}_m \\ \mathbf{f} \end{Bmatrix} \tag{12}$$

Considering the periodicity of resonators and voids inside FGAS, the periodic boundary condition of sound pressure and displacement is expressed as:

$$\chi(x + d_x, y + d_y, z) = \chi(x, y, z)e^{jd_x k \sin\theta \cos\varphi} e^{jd_y k \sin\theta \sin\varphi} \tag{13}$$

where $\chi$ denotes the sound pressure $p$ of fluid nodes or displacement u of structure nodes, and dx and dy are the lattice sizes of a unit cell in the $x$ and $y$ directions, respectively.

Afterward, the sound transmission coefficient $T$ and sound reflection coefficient $R$ can be calculated by:

$$R = \sqrt{\sum_{k_{mn}^2 > 0} |R_{mn}|^2} \tag{14}$$

$$T = \sqrt{\sum_{k_{mn}^2 > 0} |T_{mn}|^2} \tag{15}$$

The backing of the steel plate is a semi-infinite air domain. Thus, the transmission coefficient $T$ = 0, and the sound absorption coefficient (SAC) of the FGAS is determined as:

$$\alpha = 1 - R^2 \tag{16}$$

## 3. Numerical Results and Analyses

### *3.1. Acoustic Model Validation*

The material parameters of the FGMs were obtained by the Voigt model [50,51]:

$$\xi_f = \xi_1 V_1 + \xi_2 V_2 = (\xi_1 - \xi_2)V_1 + \xi_2 \tag{17}$$

where $\xi$ donates material parameters.

$V_1$ is the volume fraction of each material $h$ and can be described as:

$$\mathrm{FGM}_{\mathrm{I}(a/b/c/P)} : V_1 = [1 - a(\frac{z}{h}) + b(\frac{z}{h})^c]^P \tag{18}$$

$$\mathrm{FGM}_{\mathrm{II}(a/b/c/P)} : V_1 = [1 - a(1 - \frac{z}{h}) + b(1 - \frac{z}{h})^c]^P \tag{19}$$

where $P$ is the gradient index and $h$ is the thickness of FGMs. The spatial distribution of component materials is jointly determined by the distribution parameters $a$, $b$, and $c$.

The schematic diagram of stratification for FGMs is shown in Figure 3, and the thicknesses of gradient layers 1, 2, and the steel plate are $h_1$ = 30 mm, $h_2$ = 30 mm, and $h_s$ = 10 mm, respectively. Then, gradient layers 1 and 2 are evenly stratified into $n_1$ and $n_2$ thin layers, respectively. The distribution of the material properties of the matrix of the MMSC−AS along the thickness direction is shown in Figure 4. The material properties of each component of the MMSC−AS are listed in Table 1, which were the same as those in ref. [49]. The sound speed and density of water were $c$ = 1489 m/s and $\rho_0$ = 1000 kg/m$^3$.

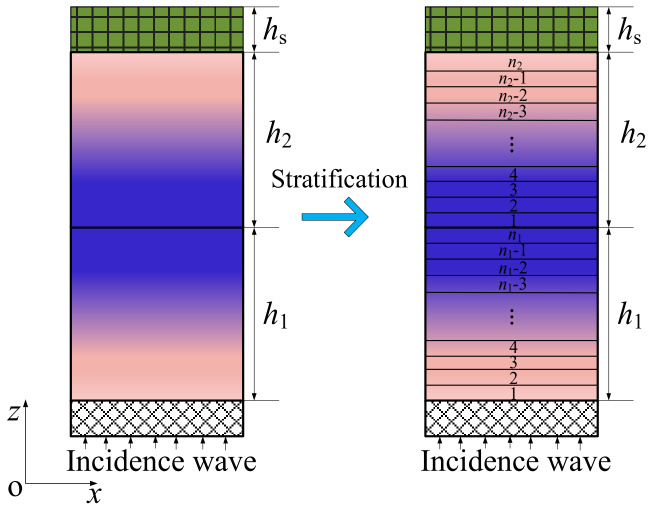


**Figure 3.** Schematic diagram of stratification for FGMs.

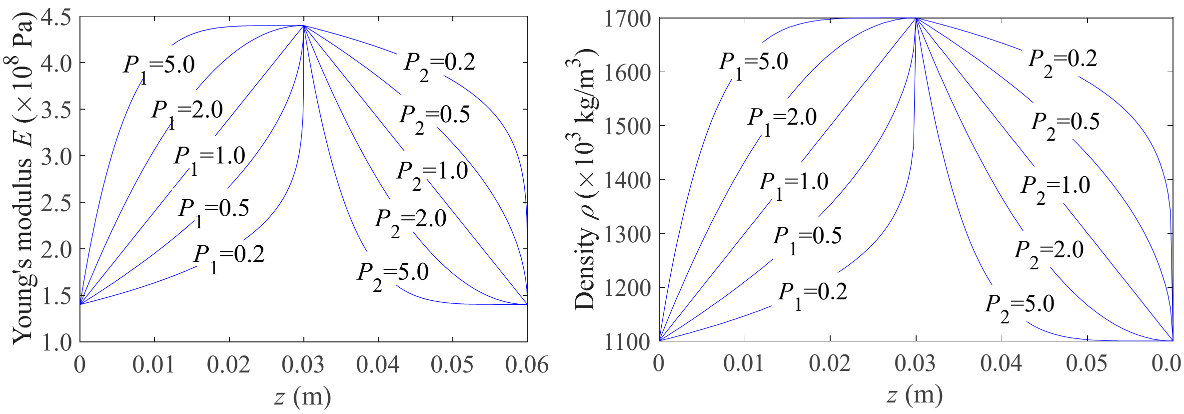


(**a**) Equivalent modulus (**b**) Equivalent density

**Figure 4.** The gradient distribution of the material properties of the matrix of the MMSC−AS along the *z* direction.

**Table 1.** Material parameters of MMSC−AS.

| Materials | | Density (kg/m$^3$) | Young's Modulus (Pa) | Poisson's Ratio | Loss Factor |
|---|---|---|---|---|---|
| Impedance match layer | Epoxy | 1100 | $1.4 \times 10^8$ | 0.49 | 0.6 |
| Functionally graded layer | Epoxy | 1100 | $1.4 \times 10^8$ | 0.49 | 0.6 |
| | Inorganic fillers | 1700 | $3.4 \times 10^8$ | 0.49 | 0.6 |
| Steel plate backing | Steel | 7800 | $2.07 \times 10^{11}$ | 0.3 | 0 |

As displayed in Figure 3, gradient layers 1 and 2 can be evenly divided into $n_1 = n_2 = 1000$ thin layers. The acoustic coefficients obtained through the transfer matrix method (TMM), FEM, and G-FEM are displayed in Figures 5 and 6. It can be found that the acoustical coefficient curves obtained through the FEM and G-FEM were consistent with those obtained through the TMM. It proves that the G-FEM computation program is correct (The program runs in software Python2.7). However, the deviations between the TMM and FEM were obvious in the high frequency when $P_1 = 5.0$ and $P_2 = 5.0$, while the acoustic coefficients obtained through the G-FEM were consistent with TMM in the high frequency. Therefore, the accuracy of the G-FEM was better than that of the FEM when the number of mesh elements was the same.

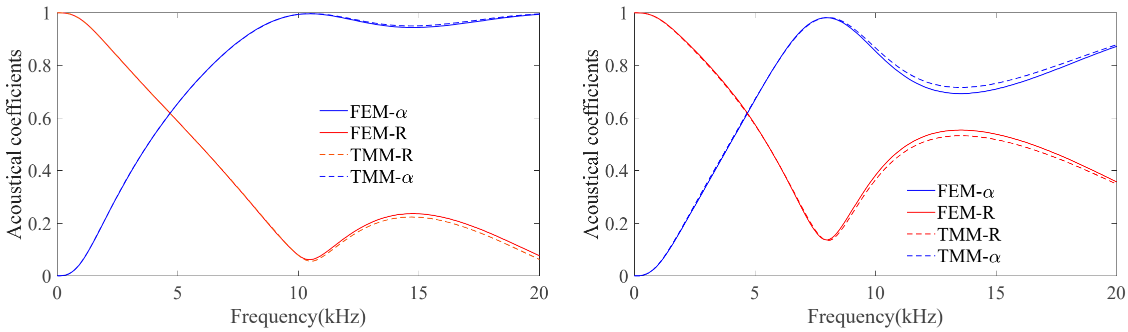


**(a)** $P_1 = 0.5$, $P_2 = 0.5$ **(b)** $P_1 = 5.0$, $P_2 = 5.0$

**Figure 5.** Acoustic coefficients calculated by FEM and TMM.

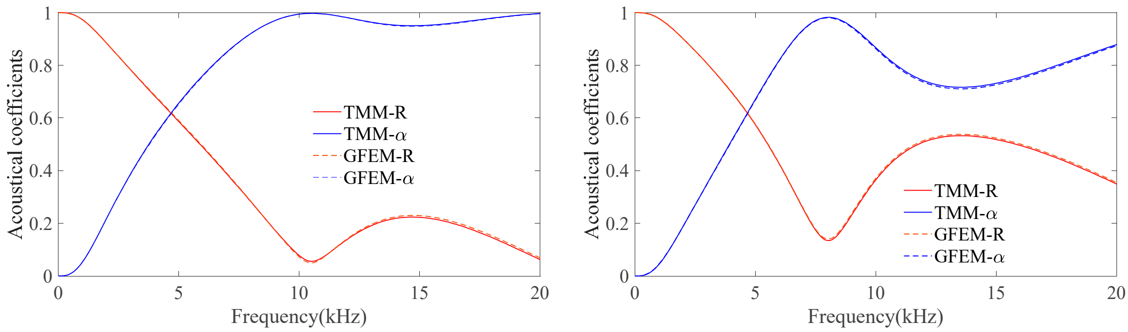


**(a)** $P_1 = 0.5$, $P_2 = 0.5$ **(b)** $P_1 = 5.0$, $P_2 = 5.0$

**Figure 6.** Acoustic coefficients calculated by TMM and GFEM.

### *3.2. Sound Absorption Characteristics of the MMSC−AS*

In Figure 2, the thicknesses of gradient layers 1 and 2 and the steel plate were set as $h_1$ = 30 mm, $h_2$ = 30 mm, and $h_s$ = 5 mm, and the radii of multi-layered spherical resonators and coating layers were $r_1$ = 12 mm, $r_2$ = 11 mm, $r_3$ = 9.5 mm, $r_4$ = 8.5 mm, $r_5$ = 7 mm, $r_6$ = 6 mm, $r_7$ = 12 mm, and $r_8$ = 10 mm, respectively. The geometrical parameters of the cavity were $r_{c1}$ = 8 mm, $h_{c1}$ = 20 mm, $r_{c2}$ = 12 mm, and $h_{c1}$ = 20 mm, and the lattice constants were set as $a_1$ = 30 mm and $a_2$ = 30 mm. The SAC of the MMSC−AS could be obtained on the basis of the acoustic calculation model.

Figure 7 shows the SAC curves of the MMSC−AS with the changes in $P_1$ and $P_2$. The SAC of the MMSC−AS at low frequencies was not affected by the changes in $P_1$ and $P_2$, while those in the high-frequency range increased with the increase in the gradient index. Therefore, the sound absorption band of the MMSC−AS could be broadened by increasing the gradient index.

When $P_1$ = 5.0 and $P_2$ = 5.0, the vibration mode of MMSC−AS at various frequencies is shown in Figure 8. It can be seen that, when f = 1010 Hz, corresponding to the first sound absorption peak (SAP), the vibration energy is mainly concentrated in the resonators in the low-frequency range, and the modulation of MMSC−AS on sound waves is mainly through the local resonance of resonators. As the frequency increases, when f = 1210 Hz and f = 1710 Hz (the second SAP), the vibration energy is mainly concentrated on gradient layers 1 and 2, the steel plate, and resonators, respectively, and the sound waves are modulated by the bending vibration of gradient layer and steel plate, coupling resonance between the multi-resonator and cavity resonance. In contrast, in the high-frequency range, when f = 4110 Hz (the third SAP) and f = 9110 Hz, the structural vibration energy was mainly concentrated in gradient layer 1, and the effect of MMSC−AS on sound waves was mainly through the bending vibration of gradient layer 1, which converted longitudinal waves into transverse waves. Therefore, the synergistic effect between the mechanisms enriched the sound wave modulation modes because of the multiple sound wave modulation mechanisms inside the MMSC−AS, and the sound absorption band could be broadened with effect.

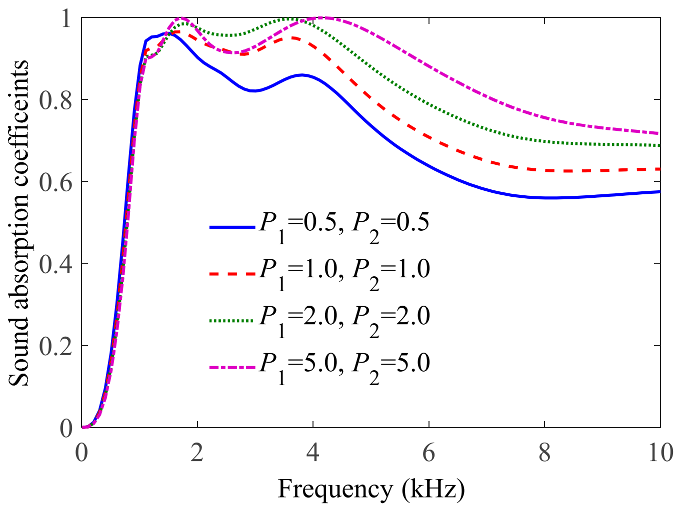


**Figure 7.** SAC of the MMSC−AS with the changes in $P_1$ and $P_2$.

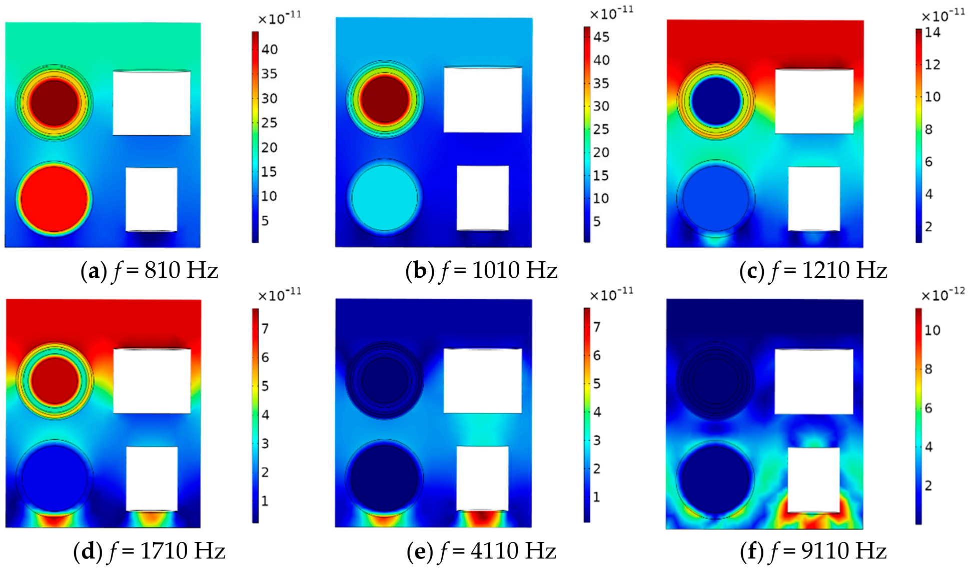


**Figure 8.** Structural vibration modes of the MMSC−AS at various frequencies.

To illustrate the synergistic mechanisms effect of local resonance, multi-resonator coupling resonance, and cavity resonance in the MMSC−AS, the geometric model of a cell of the FGAS with only resonators or cavities is displayed in Figure 9a,b, and the geometric parameters of the resonators and cavities in Figure 9a,b are the same as those in Figure 2.

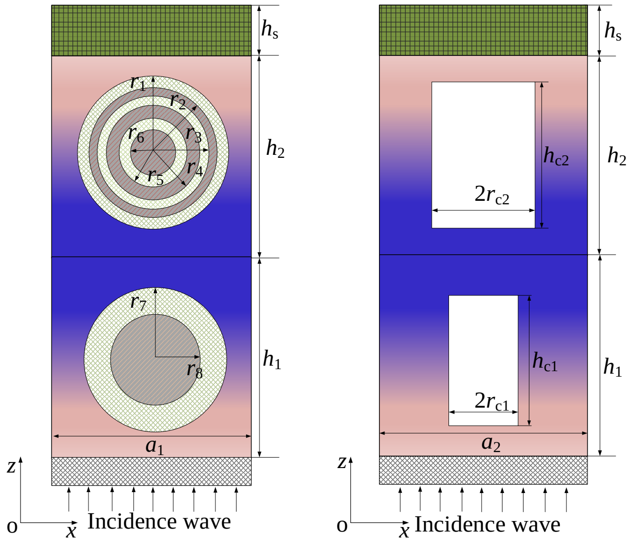


(**a**) Multi-resonator coupling (**b**) Cavity resonance

**Figure 9.** Composite functionally graded acoustic structure containing resonator and cavity structure.

The SAC curves of the three acoustic structures under various gradient indexes are displayed in Figure 10. By comparing the SAC of the three acoustic structures, the sound absorption performance of the FGAS with resonators was better than that of the FGAS with cavities at low frequencies, while the sound absorption characteristics of the FGAS with cavities were better than those of the FGAS with resonators at high frequencies. The MMSC−AS combined the characteristics of the FGAS with cavities and resonators. Due to the local resonance of resonators, the sound absorption characteristics of MMSC−AS were better than those of FGAS with the cavity at low frequencies.

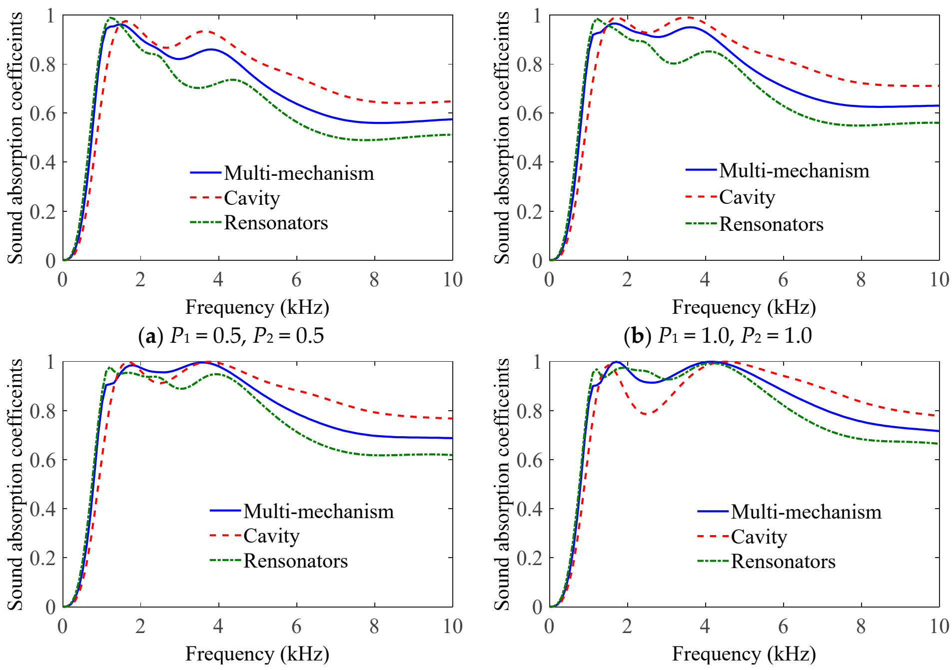


(**a**) $P_1 = 0.5$, $P_2 = 0.5$ (**b**) $P_1 = 1.0$, $P_2 = 1.0$

(**c**) $P_1 = 2.0$, $P_2 = 2.0$ (**d**) $P_1 = 5.0$, $P_2 = 5.0$

**Figure 10.** Comparison of SAC of the three acoustic structures.

### 3.3. The Effects of Sound Absorption Characteristics

The effects of $P_1$ and $P_2$ on the SAC of MMSC−AS were studied. The effect of $P_1$ on the SAC of the MMSC−AS is displayed in Figure 11. The sound absorption characteristics of the MMSC−AS at low frequencies were not affected by the change in $P_1$, the frequency of the first SAP was almost unchanged, and the second and the third SAPs moved to high frequencies.

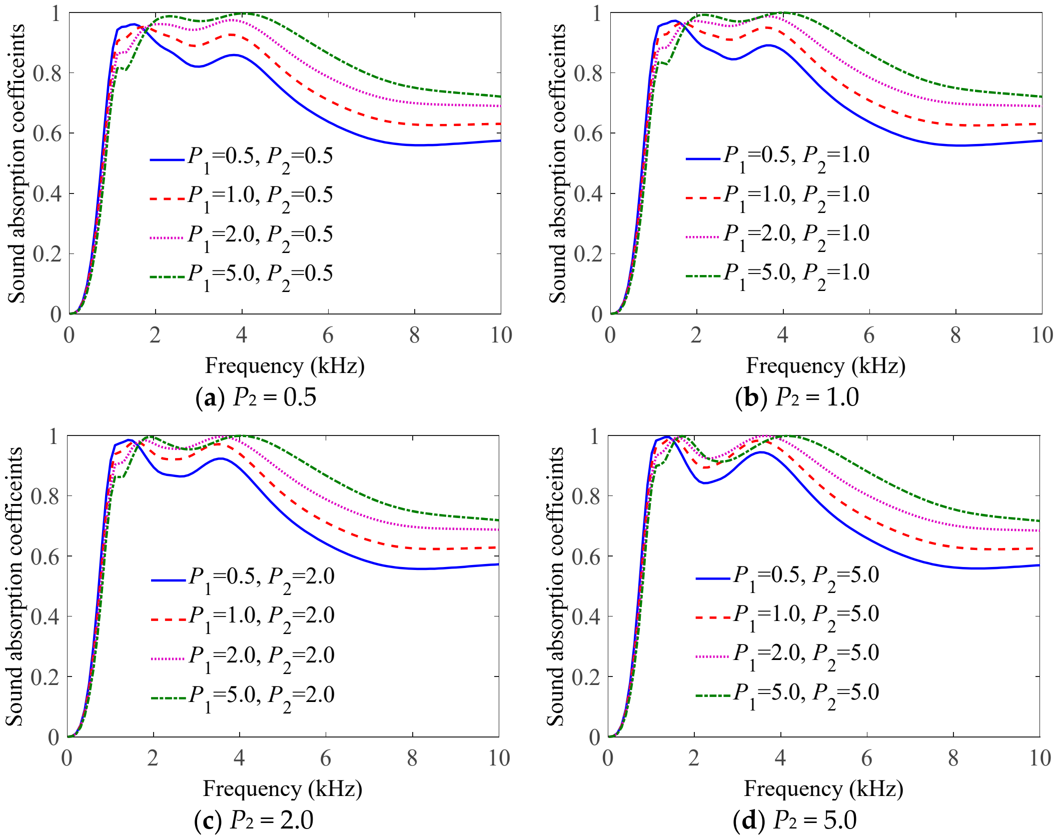


**Figure 11.** SAC of the MMSC−AS with the change in $P_1$.

Figure 12 shows the effect of $P_2$ on the SAC of the MMSC−AS. The acoustic characteristics of the MMSC−AS at low frequencies were not affected by $P_2$, and the frequency corresponding to the first SAP was almost unchanged. However, the second and third SAPs moved to the low frequency, and the absorption coefficients of the MMSC−AS in the high-frequency band remained unchanged.

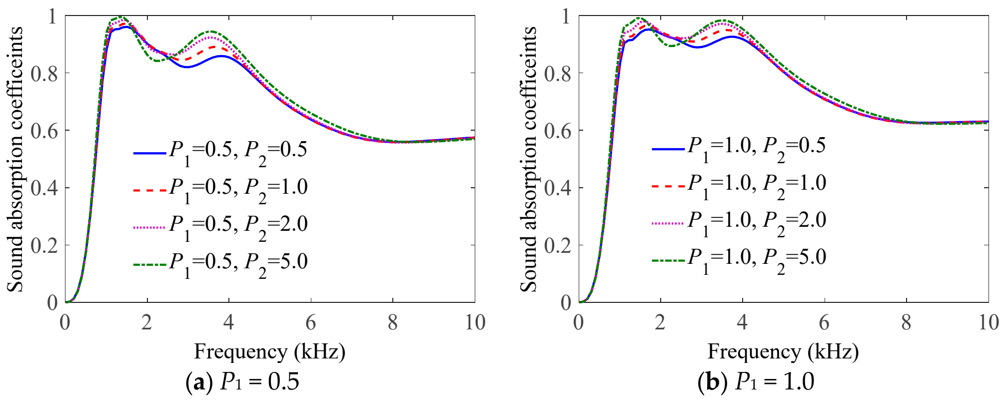


**Figure 12.** *Cont.*

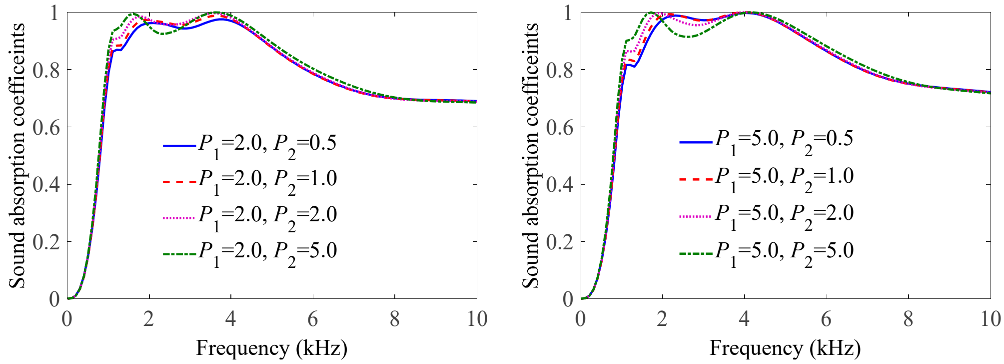


(**c**) $P_1 = 2.0$ (**d**) $P_1 = 5.0$

**Figure 12.** SAC of the MMSC−AS with the change in $P_2$.

According to the vibration mode of the MMSC−AS displayed in Figure 8, the energy of structural vibration was mainly concentrated in resonators at low frequencies, and the modulation of MMSC−AS on sound waves was mainly through the local resonance of resonators. Therefore, the gradient indexes $P_1$ and $P_2$ of the matrix material had no effect on the sound absorption performance of the MMSC−AS at low frequencies. At the frequency corresponding to the second SAP, the effect of the MMSC−AS on sound waves mainly occurred through the bending vibration effect of functional gradient layers 1 and 2, multi-vibrator coupling resonance effect, and cavity resonance effect. Additionally, at the peak frequency corresponding to the third SAP frequency, the effect of MMSC−AS on sound waves mainly occurred through the bending vibration of gradient layer 1 and cavity resonance. It can be seen that, with the increase in $P_1$, the equivalent stiffness of gradient layer 1 increased, causing the second and third SAPs to move to the high frequency. In addition, the increase in the equivalent Young's modulus of gradient layer 1 increased the acoustical impedance of the material and enhanced the dissipation of the high-frequency sound wave.

Similarly, increasing $P_2$ decreased the equivalent stiffness of gradient layer 2. Therefore, increasing $P_2$ caused the second and third SAPs of the MMSC−AS to move to lower frequencies. The change in $P_2$ did not affect the material properties of gradient layer 1, so the SAC of the MMSC−AS at high frequencies remained unchanged. Additionally, the second SAP of the MMSC−AS shifted to lower frequencies, which enhanced the coupling between the first and second SAPs, increasing the absorption coefficient of the first SAP.

The change in the SAC of MMSC−AS with the cavity radius $r_{c1}$ is shown in Figure 13. It can be found that, as the cavity radius $r_{c1}$ of gradient layer 1 increased, the sound absorption performance of the MMSC−AS at low frequencies was almost unaffected, and the frequency of the first SAP was almost unchanged. However, the second and the third SAPs both shifted to lower frequencies, which increased the value of the first SAP, and the absorption coefficients of the MMSC−AS decreased at high frequencies.

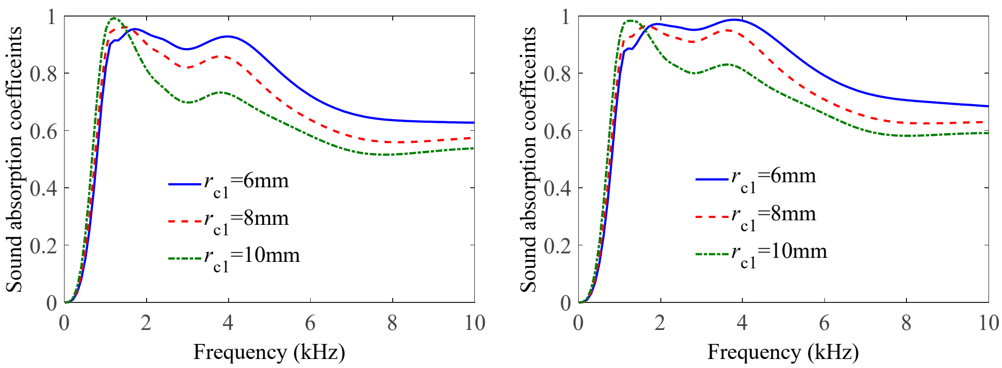


(**a**) $P_1 = 0.5$, $P_2 = 0.5$ (**b**) $P_1 = 1.0$, $P_2 = 1.0$

**Figure 13.** *Cont*.

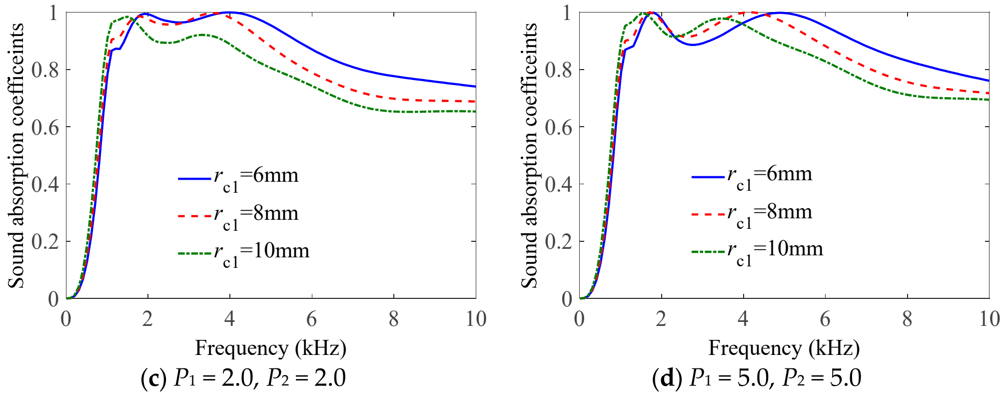


**Figure 13.** The changes in the SAC of MMSC−AS with the cavity radius $r_{c1}$.

Figure 14 displays the effect of the cavity radius $r_{c2}$ of gradient layer 2 on the SAC of the MMSC−AS under various gradient indexes. With the increase in the cavity radius $r_{c2}$ of gradient layer 2, the frequency corresponding to the first SAP was almost unchanged, and the second SAP moved to lower frequencies. Furthermore, the third SAP moved to lower frequencies with the increase in the cavity radius $r_{c2}$ of gradient layer 2, and the sound absorption performance of the MMSC−AS at high frequencies was rarely affected.

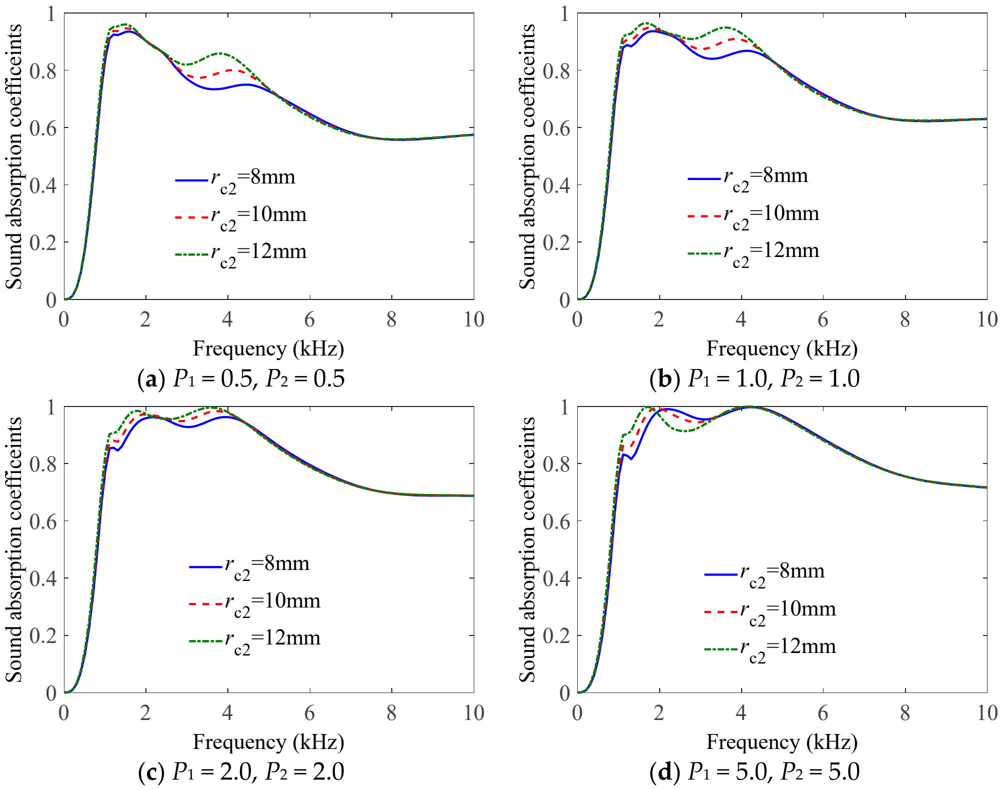


**Figure 14.** The changes in the SAC of MMSC−AS with cavity radius $r_{c2}$.

The modulation of the MMSC−AS on sound waves mainly occurs through the local resonance of resonators at low frequencies. Therefore, the change in cavity radii $r_{c1}$ and $r_{c2}$ of the matrix in the gradient layers 1 and 2 had no effect on the sound absorption performance of the MMSC−AS at low frequencies. The second and third SAPs of the MMSC−AS moved to lower frequencies with the increases in the cavity radius $r_{c1}$, while the second SAP of the MMSC−AS moved toward the lower frequencies with increases in the cavity radius $r_{c2}$. The second SAP of MMSC−AS shifted to lower frequencies, which enhanced the coupling between the first and second SAPs, increasing the value of the first

SAP. In addition, the energy dissipation for high-frequency sound waves occurred through material damping, and the acoustical impedance of the matrix decreased with the increase in the cavity radius $r_{c1}$ of gradient layer 1. Therefore, the increase in the cavity radius $r_{c1}$ reduced the SAC of the MMSC−AS at high frequencies.

The effect of the resonator distribution of gradient layers 1 and 2 on the SAC of the MMSC−AS was investigated, and the schematic diagram of MMSC−AS with different resonator distribution forms is shown in Figure 15. It can be seen that both gradient layers 1 and 2 contained a single resonator, as shown in Figure 15a, named S-S. As shown in Figure 15b, gradient layer 1 contained a multi-resonator, while gradient layer 2 contained a single resonator, named M-S. As for Figure 15c, both gradient layers 1 and 2 contained multi-resonators, named M-M, and it was named S-M for the MMSC−AS displayed in Figure 2. The filling rate and geometric parameters of the resonators of the four units were the same, respectively.

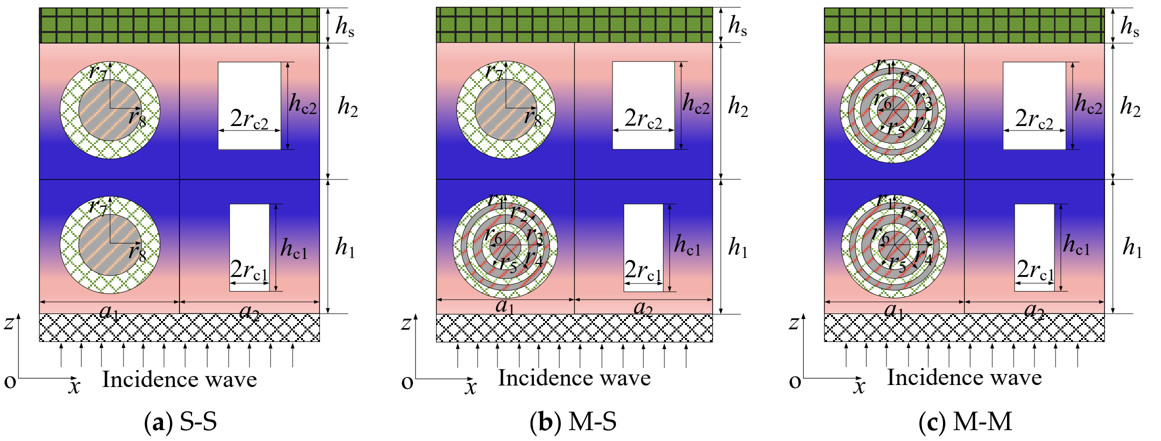


**Figure 15.** Cross-sectional view of a unit cell of the MMSC−AS with different resonator distribution forms on the *xoz* plane.

When $P_1$ = 5.0 and $P_2$ = 5.0, the SAC of the MMSC−AS with different resonator distributions are displayed in Figure 16. It can be found that, when the multi-resonator was embedded in gradient layer 1, the frequencies corresponding to the first and second SAPs of the MMSC−AS were basically unchanged compared with S-S, and the absorption coefficient of the MMSC−AS increased at high frequencies. In Figure 16b, when the multi-resonator was embedded in gradient layer 2, the first and second SAPs of MMSC−AS moved to higher frequencies, while the frequency corresponding to the third SAP basically remained unchanged compared with S-S, and the absorption coefficient of the MMSC−AS at high frequencies basically remained unchanged. By comparing S-M with M-M, it can be observed from Figure 16c that, when the distribution of resonators inside gradient layer 1 was changed, the acoustic absorption behavior of the MMSC−AS at low frequencies was basically not affected. Additionally, the third SAP moved to higher frequencies, and the SAC of the MMSC−AS at high frequencies increased. In contrast, by comparing M-S with M-M, it can be found from Figure 16d that, when the distribution of resonators inside gradient layer 2 changed, the first and second SAPs of the MMSC−AS moved to higher frequencies.

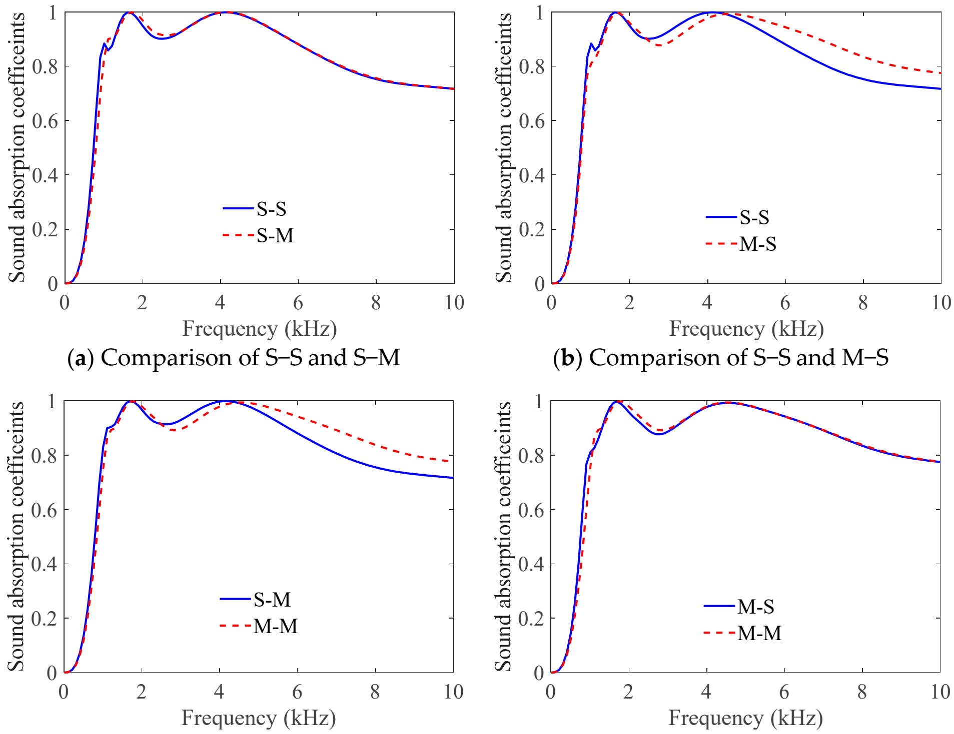


(**a**) Comparison of S–S and S–M (**b**) Comparison of S–S and M–S

(**c**) Comparison of S–M and M–M (**d**) Comparison of M–S and M–M

**Figure 16.** SAC of the MMSC−AS with different resonator distributions when $P_1$ = 5.0 and $P_2$ = 5.0.

### 3.4. Optimization of Sound Absorption Characteristics

The optimization of the sound absorption characteristics of MMSC−AS was carried out based on the Nelder–Mead algorithm. The objective function of the Nelder–Mead algorithm is not required to be differentiable, and the algorithm can be applied when the objective function is discontinuous or error exists [52]. This algorithm is usually applied to nonlinear optimization problems where the derivative of the objective function may be unknown. The objective function of the acoustic performance optimization of the MMSC−AS can be expressed as

$$\begin{cases} find : \mathbf{x} = (P_1, P_2, r_{c1}, r_{c2}, h_{c1}, h_{c2}, E, \rho, \nu, \eta) \\ \quad obj(\mathbf{x}) = \max \bar{\alpha}_{0.5\text{kHz}-10\text{kHz}} \\ \quad S.t.\mathbf{x}_{\min} \leq \mathbf{x} \leq \mathbf{x}_{\max} \end{cases} \tag{20}$$

where $\mathbf{x}$ represents the design variables and $obj(\mathbf{x})$ donates the objective function.

According to the sound absorption characteristics analysis in Section 3.2, the cavity radii $r_{c1}$ and $r_{c2}$ of gradient layers 1 and 2 were important considerations affecting the sound absorption characteristics of the MMSC−AS. Taking the geometric parameters of the cavity of the MMSC−AS as variables, the range of geometric parameters for the cavities of gradient layers 1 and 2 and the selection of initial values are shown in Table 2. Taking $P_1$ = 2.0, $P_2$ = 2.0 and $P_1$ = 5.0, $P_2$ = 5.0 as examples, the optimization of the sound absorption characteristics is carried out in software COMSOL5.6, and the optimal solution of the geometric parameters and the SAC after optimization can be achieved.

**Table 2.** The ranges of geometric parameters and initial values.

| Variables | $r_{c11}$/mm | $r_{c12}$/mm | $h_{c1}$/mm | $r_{c21}$/mm | $r_{c22}$/mm | $h_{c1}$/mm |
|---|---|---|---|---|---|---|
| Range | [3, 10] | [3, 10] | [10, 25] | [3, 12] | [3, 12] | [10, 25] |
| Initial value | 8 | 8 | 20 | 12 | 12 | 20 |

When gradient indexes $P_1$ = 2.0 and $P_2$ = 2.0, the geometric parameters of MMSC−AS after optimization were $r_{c11}$ = 4.4 mm, $r_{c12}$ = 4.4 mm, $h_{c1}$ = 25.0 mm, $r_{c21}$ = 10.2 mm, $r_{c22}$ = 9.7 mm, and $h_{c2}$ = 22.1 mm, and the comparison of SAC before and after optimization of the MMSC−AS is shown in Figure 17a. When gradient indexes $P_1$ = 5.0 and $P_2$ = 5.0, the geometric parameters of the MMSC−AS after optimization were $r_{c11}$ = 6.2 mm, $r_{c12}$ = 6.2 mm, $h_{c1}$ = 21.1 mm, $r_{c21}$ = 10.5 mm, $r_{c22}$ = 8.8 mm, and $h_{c2}$ = 25.0 mm. A comparison of SAC of MMSC−AS before and after optimization is displayed in Figure 17b.

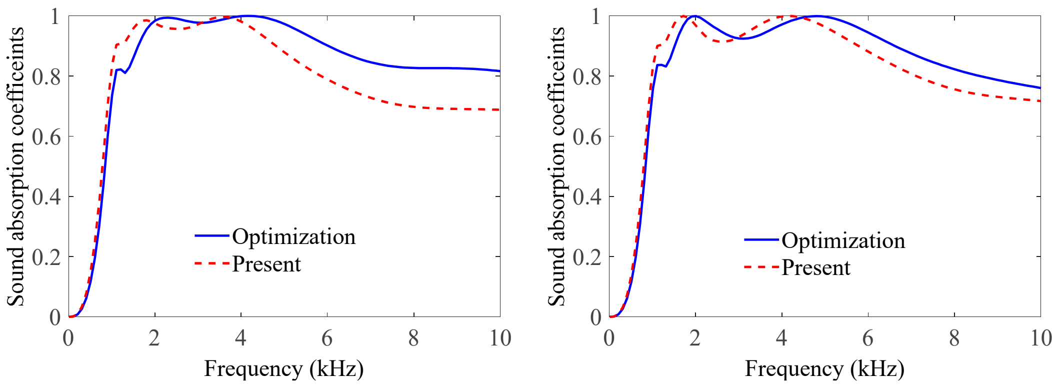


(**a**) $P_1 = 2.0$, $P_2 = 2.0$ (**b**) $P_1 = 5.0$, $P_2 = 5.0$

**Figure 17.** SAC of MMSC−AS before and after geometric optimization.

As shown in Figure 17, the average SAC of the MMSC−AS in the range of 0.1–10 kHz was approximately 0.8298 ($P_1$ = 2.0, $P_2$ = 2.0) and 0.8269 ($P_1$ = 5.0, $P_2$ = 5.0) by optimizing the geometric parameters of the cavities of gradient layers 1 and 2, respectively. In addition, by optimizing the geometric parameters of the cavities of gradient layers 1 and 2, the sound absorption characteristics of the MMSC−AS were obviously improved at high frequencies, but the sound absorption characteristics at low frequencies were almost unchanged. This was mainly due to the fact that the effect of the MMSC−AS on sound waves was mainly through the local resonance of resonators. Therefore, optimizing the geometric parameters of the cavities of gradient layers 1 and 2 had almost no influence on the sound absorption behavior of the MMSC−AS at low frequencies.

The material parameters to be optimized are listed in Table 3. The geometric parameters of MMSC−AS were invariant, which is the same as the data in Figure 2. The value range of material parameters to be optimized and the selection of initial values are shown in Table 3, and the optimization of structural parameters of MMSC−AS was carried out.

**Table 3.** The range of the parameters of the materials and initial values.

| **Variables** | **Young's Modulus (Pa)** | **Density (kg/m$^3$)** | **Poisson's Ratio** | $P_1$ | $P_2$ |
|---|---|---|---|---|---|
| Range | [2.4, 5.4] $\times 10^8$ | [2.1, 4.1] $\times 10^3$ | [0.45, 0.49] | [0.5, 5.0] | [0.5, 5.0] |
| Initial value | $2.4 \times 10^8$ | 3100 | 0.45 | 1.0 | 1.0 |

The optimized material parameters were Young's modulus $E = 5.4 \times 10^8$ Pa, density $\rho$ = 2863 kg/m$^3$, Poisson ratio $\nu$ = 0.49, gradient indexes $P_1$ = 5.0, and $P_2$ = 4.13, respectively. The SACs of the MMSC−AS before and after optimization are shown in Figure 18. The SAPs at low frequencies were almost unchanged, and the third SAP shifted to higher frequencies. The sound absorption performance of the MMSC−AS at high frequencies was significantly improved after the optimization of the material parameters of the MMSC−AS. According to the sound absorption mechanism of the MMSC−AS, the effect of the MMSC−AS on sound waves mainly occurred through local resonance. Therefore, the optimization of material parameters of the MMSC−AS had almost no influence on the acoustic absorption coefficients at low frequencies.

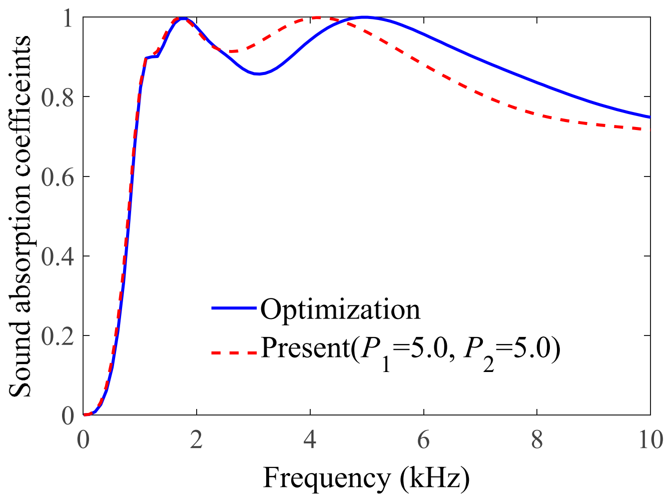


**Figure 18.** SAC of the MMSC−AS before and after material optimization.

When the geometric and material parameters of MMSC−AS were optimized simultaneously, the optimized material parameters and geometric parameters were Young's modulus $E = 5.4 \times 10^8$ Pa, density $\rho = 3100$ kg/m$^3$, Poisson ratio $\nu = 0.45$, gradient index $P_1 = 5.0$, $P_2 = 2.0$, $r_{c11} = 3.0$ mm, $r_{c12} = 3.0$ mm, $h_{c1} = 10$ mm, $r_{c21} = 3.0$ mm, $r_{c22} = 3.0$ mm, and $h_{c2} = 10$ mm, respectively. The sound absorption curves before and after the comprehensive optimization of the MMSC−AS are shown in Figure 19, the frequency corresponding to the first SAP was almost immutable, the second and third sound SAPs shifted to higher frequencies after the comprehensive optimization of the SAC of MMSC−AS, and the SAC increased notably at high frequencies.

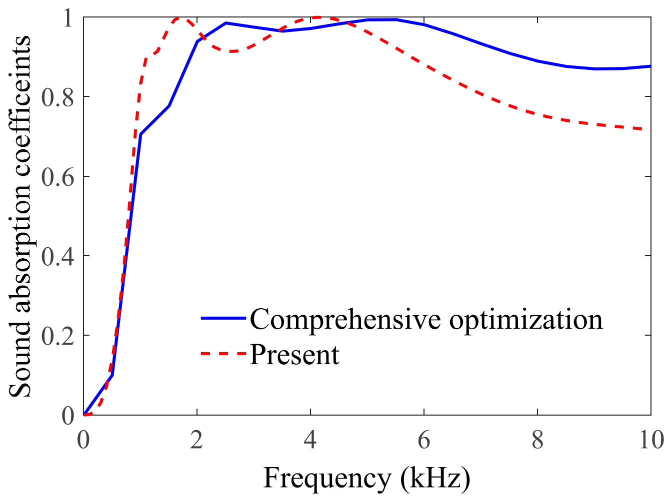


**Figure 19.** SAC of the MMSC−AS before and after comprehensive optimization.

By comparing the MMSC−AS before and after optimization, the structural equivalent impedance increased as the structural modulus increased and the gradient index $P_2$ decreased after optimization, which is the reason for the SAC of MMSC−AS increasing at high frequencies. Moreover, the coupling effect between the first and second acoustic peaks was weakened as a result of the deviation of the second SAP of the MMSC−AS moving to higher frequencies, which reduced the first SAP value.

## 4. Conclusions

In this study, a new type of MMSC−AS was designed on the basis of multiple sound absorption mechanisms, such as local resonance, multi-resonator coupling resonance, cavity resonance, and FGMs, and the G-FEM was used to develop the acoustic model of the MMSC−AS. The following conclusions could be obtained by analyzing the numerical results systematically.

(1) The accuracy of the G-FEM was better than that of the FEM when calculating the acoustic coefficients of the FGAS under the condition of the same number of finite elements meshes;
(2) Owing to the presence of multiple sound wave modulation mechanisms inside the MMSC−AS, the synergy between various mechanisms enriched the energy dissipation modes of sound waves, which widened the sound absorption frequency band with effect, thus achieving the underwater low-frequency and broadband sound absorption performance;
(3) The MMSC−AS could be regulated by adjusting material or structural parameters that affect sound absorption characteristics based on the sound wave modulation mechanism of the MMSC−AS in different frequency bands;
(4) The sound absorption characteristics of the MMSC−AS could be effectively ameliorated by optimizing the material or the structural parameters, while the sound absorption characteristics at low frequencies could be ameliorated by optimizing the distribution or filling ratio of the resonators.

This study suggests that the low-frequency broadband underwater sound absorption performance could be achieved by the proposed MMSC−AS, which provides a novel approach for the practical application in acoustic stealth of underwater vehicles.

**Author Contributions:** Conceptualization, K.S. and G.J.; Methodology, D.H.; Software, D.L. and Q.S.; Validation, K.S.; Formal analysis, D.H.; Investigation, K.S., D.L. and Q.S.; Data curation, D.H. and Q.S.; Writing—original draft, K.S.; Visualization, D.L.; Supervision, G.J.; Funding acquisition, D.L. and G.J. All authors have read and agreed to the published version of the manuscript.

**Funding:** This research was funded by National Natural Science Foundation of China grant numbers U2141244 and 52225109.

**Institutional Review Board Statement:** Not applicable.

**Informed Consent Statement:** Not applicable.

**Data Availability Statement:** No new data were created or analyzed in this study. Data sharing is not applicable to this article.

**Acknowledgments:** The authors appreciate the kind support from China Ship Scientific Research Center, Taihu Laboratory of Deepsea Technological Science, and Harbin Engineering University.

**Conflicts of Interest:** The authors declare no conflict of interest.

## References

1. Wang, X.; Guo, L.; Yin, J.; Liu, Z.; Han, X. Narrowband Chan-Vese model of sonar image segmentation: A adaptive ladder initialization approach. *Appl. Acoust.* **2016**, *113*, 238–254. [CrossRef]
2. Wang, X.; Jiao, J.; Yin, J.; Zhao, W.; Han, X.; Sun, B. Underwater sonar image classification using adaptive weights convolutional neural network. *Appl. Acoust.* **2019**, *146*, 145–154. [CrossRef]
3. Hosten, B.; Castaings, M. Transfer matrix of multilayered absorbing and anisotropic media. Measurements and simulations of ultrasonic wave propagation through composite materials. *J. Acoust. Soc. Am.* **1993**, *94*, 1488–1495. [CrossRef]
4. Cervenka, P.; Challande, P. A new efficient algorithm to compute the exact reflection and transmission factors for plane waves in layered absorbing media (liquids and solids). *J. Acoust. Soc. Am.* **1991**, *89*, 1579–1589. [CrossRef]
5. Sastry, J.; Munjal, M. Response of a Multi-Layered Infinite Cylinder to a Plane Wave Excitation by Means of Transfer Matrices. *J. Sound Vib.* **1998**, *209*, 99–121. [CrossRef]
6. Gaunaurd, G. One-dimensional model for acoustic absorption in a viscoelastic medium containing short cylindrical cavities. *J. Acoust. Soc. Am.* **1977**, *62*, 298–307. [CrossRef]
7. Kerr, F.H. The scattering of a plane elastic wave by spherical elastic inclusions. *Int. J. Eng. Sci.* **1992**, *30*, 169–186. [CrossRef]

8. Brouard, B.; Lafarge, D.; Allard, J.-F. A general method of modelling sound propagation in layered media. *J. Sound Vib.* **1995**, *183*, 129–142. [CrossRef]
9. Sharma, G.S.; Skvortsov, A.; MacGillivray, I.; Kessissoglou, N. Sound transmission through a periodically voided soft elastic medium submerged in water. *Wave Motion* **2017**, *70*, 101–112. [CrossRef]
10. Sharma, G.S.; Skvortsov, A.; MacGillivray, I.; Kessissoglou, N. Acoustic performance of gratings of cylindrical voids in a soft elastic medium with a steel backing. *J. Acoust. Soc. Am.* **2017**, *141*, 4694–4704. [CrossRef]
11. Sharma, G.S.; Skvortsov, A.; MacGillivray, I.; Kessissoglou, N. Sound absorption by rubber coatings with periodic voids and hard inclusions. *Appl. Acoust.* **2019**, *143*, 200–210. [CrossRef]
12. Meng, T. Simplified model for predicting acoustic performance of an underwater sound absorption coating. *J. Vib. Control.* **2012**, *20*, 339–354. [CrossRef]
13. Hasheminejad, S.M.; Maleki, M. Interaction of a plane progressive sound wave with a functionally graded spherical shell. *Ultrasonics* **2006**, *45*, 165–177. [CrossRef] [PubMed]
14. Hasheminejad, S.M.; Rajabi, M. Acoustic resonance scattering from a submerged functionally graded cylindrical shell. *J. Sound Vib.* **2007**, *302*, 208–228. [CrossRef]
15. Liu, Z.; Zhang, X.; Mao, Y.; Zhu, Y.Y.; Yang, Z.; Chan, C.T.; Sheng, P. Locally Resonant Sonic Materials. *Science* **2000**, *289*, 1734–1736. [CrossRef] [PubMed]
16. Liu, Z.; Chan, C.T.; Sheng, P. Analytic model of phononic crystals with local resonances. *Phys. Rev. B* **2005**, *71*, 014103. [CrossRef]
17. Li, J.; Chan, C.T. Double-negative acoustic metamaterial. *Phys. Rev. E* **2004**, *70*, 055602. [CrossRef]
18. Lai, Y.; Wu, Y.; Sheng, P.; Zhang, Z.-Q. Hybrid elastic solids. *Nat. Mater.* **2011**, *10*, 620–624. [CrossRef]
19. Yang, Z.; Mei, J.; Yang, M.; Chan, N.H.; Sheng, P. Membrane-Type Acoustic Metamaterial with Negative Dynamic Mass. *Phys. Rev. Lett.* **2008**, *101*, 204301. [CrossRef]
20. Xiao, Y.; Wen, J.; Wen, X. Sound transmission loss of metamaterial-based thin plates with multiple subwavelength arrays of attached resonators. *J. Sound Vib.* **2012**, *331*, 5408–5423. [CrossRef]
21. Mei, J.; Ma, G.; Yang, M.; Yang, Z.; Wen, W.; Sheng, P. Dark acoustic metamaterials as super absorbers for low-frequency sound. *Nat. Commun.* **2012**, *3*, 756. [CrossRef] [PubMed]
22. Wang, X.; Luo, X.; Zhao, H.; Huang, Z. Acoustic perfect absorption and broadband insulation achieved by double-zero metamaterials. *Appl. Phys. Lett.* **2018**, *112*, 021901. [CrossRef]
23. Lu, K.; Wu, J.H.; Guan, D.; Gao, N.; Jing, L. A lightweight low-frequency sound insulation membrane-type acoustic metamaterial. *AIP Adv.* **2016**, *6*, 025116. [CrossRef]
24. Ma, F.; Wu, J.H.; Huang, M.; Zhang, W.; Zhang, S. A purely flexible lightweight membrane-type acoustic metamaterial. *J. Phys. D Appl. Phys.* **2015**, *48*, 175105. [CrossRef]
25. Ma, F.; Huang, M.; Wu, J.H. Acoustic metamaterials with synergetic coupling. *J. Appl. Phys.* **2017**, *122*, 215102. [CrossRef]
26. Ma, F.; Wang, L.; Du, P.; Wang, C.; Wu, J.H. A three-dimensional broadband underwater acoustic concentrator. *J. Phys. D Appl. Phys.* **2022**, *55*, 195110. [CrossRef]
27. Veselago, V.G.; Vinogradov, E.A.; Golovanov, V.I.; Zhukov, A.A.; Romanov, A.A.; Kapustyan, A.V.; Urlichich, Y.M.; Lavrishchev, V.P. Waveguide propagation of microwave radiation in two-layer metamaterial. *Tech. Phys. Lett.* **2011**, *37*, 220–222. [CrossRef]
28. Veselago, V.G. Waves in metamaterials: Their role in modern physics. *Physics-Uspekhi* **2012**, *54*, 1161–1165. [CrossRef]
29. Veselago, V.; Braginsky, L.; Shklover, V.; Hafner, C. Negative Refractive Index Materials. *J. Comput. Theor. Nanosci.* **2006**, *3*, 189–218. [CrossRef]
30. Wen, J.; Zhao, H.; Lv, L.; Yuan, B.; Wang, G.; Wen, X. Effects of locally resonant modes on underwater sound absorption in viscoelastic materials. *J. Acoust. Soc. Am.* **2011**, *130*, 1201–1208. [CrossRef]
31. Zhao, H.; Wen, J.; Yang, H.; Lv, L.; Wen, X. Backing effects on the underwater acoustic absorption of a viscoelastic slab with locally resonant scatterers. *Appl. Acoust.* **2014**, *76*, 48–51. [CrossRef]
32. Meng, H.; Wen, J.; Zhao, H.; Lv, L.; Wen, X. Analysis of absorption performances of anechoic layers with steel plate backing. *J. Acoust. Soc. Am.* **2012**, *132*, 69–75. [CrossRef] [PubMed]
33. Wang, Y.; Zhao, H.; Yang, H.; Zhong, J.; Yu, D.; Wen, J. Inverse design of structured materials for broadband sound absorption. *J. Phys. D Appl. Phys.* **2021**, *54*, 265301. [CrossRef]
34. Zhao, H.; Zheng, Q.; Wang, Y.; Cao, J.; Wang, C.; Wen, J. Acoustic absorption of a metamaterial panel: Mechanism, boundary effect and experimental demonstration. *Appl. Acoust.* **2021**, *184*, 108369. [CrossRef]
35. Wu, F.; Xiao, Y.; Yu, D.; Zhao, H.; Wang, Y.; Wen, J. Low-frequency sound absorption of hybrid absorber based on micro-perforated panel and coiled-up channels. *Appl. Phys. Lett.* **2019**, *114*, 151901. [CrossRef]
36. Zhang, Y.; Pan, J. Underwater sound scattering and absorption by a coated infinite plate with a distributed inhomogeneity. *J. Acoust. Soc. Am.* **2013**, *133*, 2082–2096. [CrossRef] [PubMed]
37. Zhang, Y.; Huang, H.; Zheng, J.; Pan, J. Underwater sound scattering and absorption by a coated infinite plate with attached periodically located inhomogeneities. *J. Acoust. Soc. Am.* **2015**, *138*, 2707–2721. [CrossRef] [PubMed]
38. Zhang, Y.; Pan, J.; Chen, K.; Zhong, J. Subwavelength and quasi-perfect underwater sound absorber for multiple and broad frequency bands. *J. Acoust. Soc. Am.* **2018**, *144*, 648–659. [CrossRef]
39. Jiang, H.; Wang, Y.; Zhang, M.; Hu, Y.; Lan, D.; Zhang, Y.; Wei, B. Locally resonant phononic woodpile: A wide band anomalous underwater acoustic absorbing material. *Appl. Phys. Lett.* **2009**, *95*, 104101. [CrossRef]

40. Jiang, H.; Wang, Y. Phononic glass: A robust acoustic-absorption material. *J. Acoust. Soc. Am.* **2012**, *132*, 694–699. [CrossRef]
41. Chen, M.; Jiang, H.; Feng, Y.; Wang, Y. Investigation of locally resonant absorption and factors affecting the absorption band of a phononic glass. *Appl. Phys. A* **2014**, *117*, 2067–2072. [CrossRef]
42. Chen, M.; Meng, D.; Zhang, H.; Jiang, H.; Wang, Y. Resonance-coupling effect on broad band gap formation in locally resonant sonic metamaterials. *Wave Motion* **2016**, *63*, 111–119. [CrossRef]
43. Gao, N.; Zhang, Y. A low frequency underwater metastructure composed by helix metal and viscoelastic damping rubber. *J. Vib. Control.* **2018**, *25*, 538–548. [CrossRef]
44. Gao, N.; Zhang, Z. Optimization design and experimental verification of composite absorber with broadband and high efficiency sound absorption. *Appl. Acoust.* **2021**, *183*, 108288. [CrossRef]
45. Gao, N.; Lu, K. An underwater metamaterial for broadband acoustic absorption at low frequency. *Appl. Acoust.* **2020**, *169*, 107500. [CrossRef]
46. Gu, Y.; Zhong, H.; Bao, B.; Wang, Q.; Wu, J. Experimental investigation of underwater locally multi-resonant metamaterials under high hydrostatic pressure for low frequency sound absorption. *Appl. Acoust.* **2021**, *172*, 107605. [CrossRef]
47. Gao, N.; Yu, H.; Liu, J.; Deng, J.; Huang, Q.; Chen, D.; Pan, G. Experimental investigation of composite metamaterial for underwater sound absorption. *Appl. Acoust.* **2023**, *211*, 109466. [CrossRef]
48. Zhang, Y.; Cheng, L. Ultra-thin and broadband low-frequency underwater acoustic meta-absorber. *Int. J. Mech. Sci.* **2021**, *210*, 106732. [CrossRef]
49. Shi, K.; Hu, D.; Li, D.; Jin, G. Sound absorption behaviors of composite functionally graded acoustic structure under hydrostatic pressure. *Appl. Acoust.* **2023**, *211*, 109474. [CrossRef]
50. Tornabene, F.; Viola, E. Free vibrations of four-parameter functionally graded parabolic panels and shells of revolution. *Eur. J. Mech.—A/Solids* **2009**, *28*, 991–1013. [CrossRef]
51. Qu, Y.; Long, X.; Yuan, G.; Meng, G. A unified formulation for vibration analysis of functionally graded shells of revolution with arbitrary boundary conditions. *Compos. Part B Eng.* **2013**, *50*, 381–402. [CrossRef]
52. Abdel-Basset, M.; Mohamed, R.; Mirjalili, S. A novel Whale Optimization Algorithm integrated with Nelder–Mead simplex for multi-objective optimization problems. *Knowl.-Based Syst.* **2021**, *212*, 106619. [CrossRef]